

This article belongs to the *Special Issue on Digital Twin Empowered Internet of Intelligent Things for Engineering Cyber-Physical Human Systems* edited by C. Venkatesan, Y.-D. Zhang, Q. Xin

Microfluidic Design for Continuous Separation of Blood Particles and Plasma Using Dielectrophoretic Force Principle

Writtick PAKHIRA¹*, Rajagopal KUMAR¹),
Fenil Chetankumar PANWALA²), Khalid Mohd IBRAHIMI¹)

¹) *Department of Electronics and Instrumentation Engineering, National Institute of Technology, Nagaland, Dimapur-797103, India; e-mails: rajagopal.kumar4@gmail.com, khalid11july@gmail.com*

²) *Department of Electronics and Instrumentation Engineering, Siddaganga Institute of Technology, Tumakuru-572103, Karnataka, India; e-mail: fenilpanwala68@gmail.com*

* *Corresponding Author e-mail: writtickpakhira@gmail.com*

Nowadays, various microfluidic platforms are developed with a focus on point-of-care diagnostics in the biomedical field. Segregation of blood cells and plasma remains an essential part of medical diagnosis in which isolation of platelets (PLTs), red blood cells (RBCs), and white blood cells (WBCs) is a requirement for analysis of diseases associated with thrombocytopenia, anemia, and leukopenia. However, a separated plasma contains proteins, nucleic acids, and viruses, for which a microfluidic device is introduced for continuous separation of PLTs, RBCs, and WBCs with a diameter range of 1.8–2 μm , 5–6 μm , and 9.4–14 μm , respectively, and plasma using the negative dielectrophoresis (DEP) force principle. In this study, design of the device is explored utilizing COMSOL Multiphysics 5.4 tool. This design consists of triangular micro-tip electrodes at the top, which are effective in generating a nonuniform electrical field with a significantly small AC voltage. Furthermore, the blood cells are subjected to the negative DEP force resulting in deflection toward their respective outlets, due to which blood cell separation purity and efficiency from the sample, i.e., of PLTs, RBCs, and WBCs, improve and are obtained at a blood sample flow velocity of 700 $\mu\text{m}/\text{s}$ and buffer solution flow velocity of 1200 $\mu\text{m}/\text{s}$ with 12 V_{pp} electrode voltage, after experimenting and testing at multiple flow velocities. Additionally, a curved microchannel is introduced, producing better plasma flow velocity than a flat microchannel at the side outlets (top and bottom). The cell-free diluted plasma is collected at side outlets (top and bottom) with high purity and improved separation efficiency.

Keywords: blood cell separation, dielectrophoresis, microfluidic device, plasma separation.



Copyright © 2023 The Author(s).

Published by IPPT PAN. This work is licensed under the Creative Commons Attribution License CC BY 4.0 (<https://creativecommons.org/licenses/by/4.0/>).

1. INTRODUCTION

Human blood contains PLTs, RBCs, WBCs, and plasma. A very low PLT count leads to thrombocytopenia. A very low WBC count leads to viral infections in the body. On the other hand, an excessive WBC count may be a sign of leukemia. Also, the calculation of the RBC count anticipates the possible occurrence of diseases such as anemia, vitamin B6 and B12 deficiency. About 55% of our blood is plasma. The cell-free plasma is a slightly yellowish liquid. Blood plasma can be regarded as the core of information that comprises signs of biomarkers, including proteins, nucleic acids and pathogens for medical analysis [1]. Therefore, the most efficient approach for evaluating a patient's overall health is a blood test. In blood diagnosis, the cells in WBCs, RBCs, PLTs, and plasma are separated distinctly, and then counting and exploring of the cells and plasma is conducted for further disease analysis. The conventional approach for separating blood components is gradient centrifugation, which involves laboratory infrastructures and technical complexities [2]. Therefore, there is a need to develop new technologies with fewer complexities.

Among the several new technologies, microfluidics plays a crucial role in today's emerging medical science. Microfluidic technology utilizes a significantly small volume of biological fluids and biological particles with a size range of several micrometers using microchannels and microelectronics [3]. One of the most preferred microfluidics applications are lab-on-a-chip devices. In these microfluidic platforms, several mechanisms are used for separating the blood components. These mechanisms are classified into two broad sections of active and passive mechanisms, as given in Fig. 1 [4–6].

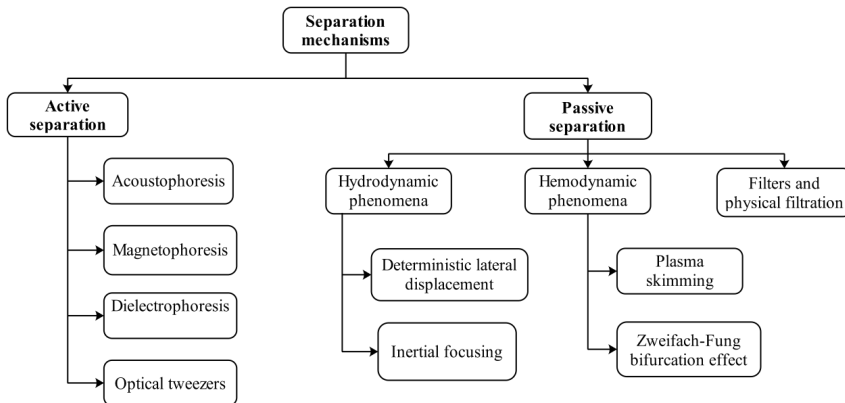


FIG. 1. Classification of separation mechanism in microfluidics.

Among the various active separation mechanisms, in acoustophoresis, ultrasonic standing wave force controls the movement of the bio-particles. In magne-

trophoresis, magnetic nanoparticles are attached to targeted biological cells, and by using magnetophoretic force in a nonuniform magnetic field, separation takes place through the deflection of cells based on their size, magnetic susceptibility, and flow velocity. In DEP, utilizing a DEP force in a non-uniform electrical field, the cells are separated based on diameter, dielectric permittivity, electrical conductivity, and flow velocity. Optical tweezers utilize focused laser beams for sorting the cells depending on their size and refractive index variance. Including several passive separation mechanisms, the hydrodynamic phenomenon is a technique in which the cells are separated based on their sizes. Other popular cell separation mechanisms are the hemodynamic phenomena and filtration techniques.

Karthick and Sen [7] developed a microfluidic blood plasma separator device utilizing the acoustophoresis mechanism. Yan *et al.* [8] designed a microfluidics device for separating the blood particles and plasma from diluted blood using the negative DEP force and achieved a plasma purity of 94.2% with a separation recovery of 16.5%. Yang *et al.* [9] designed a micro-channel for separating the plasma from whole sampled blood using DEP and got 100% purified plasma, with a separation recovery of 31%. Lee *et al.* [10] developed a diluted blood plasma separator using the inertial lift and Dean drag forces with an RBC rejection rate of 60% and plasma isolation recovery of 62.2%. Spigarelli *et al.* [11] designed a microfluidics filter-based device for low volume blood-plasma separation.

Yet, these devices only separate the plasma from blood cells and do not separate the individual blood cells along with plasma. However, Zhang *et al.* [12] designed a microfluidic chip for separating RBCs and PLTs utilizing a negative DEP force with 100% cell separation purity. Shirinkami *et al.* [13] designed a microfluidic chip for separating WBCs and RBCs using hydraulic jump and sedimentation hydrodynamic phenomena and trapped 69% of WBCs and 80% of RBCs. However, these approaches are only for separating the blood cells, not for plasma.

So, we have developed a device that can separate blood particles such as PLTs, RBCs, and WBCs and also continuously dilute plasma using the negative DEP force. Our intention was to develop a microfluidic device conducting the complete clarification in blood analysis. Different design stages, electrode shapes, voltages, and flow velocities on blood cells and plasma separation were simulated using COMSOL Multiphysics 5.4 software.

2. THEORETICAL BACKGROUND

DEP is a force that is applied on the dipole moment-induced dielectric particle with zero surface net charge using a nonuniform electrical field [14]. In the nonuniform electrical field \vec{E} , the dipole having similar and inverse charges $+q$

and $-q$ at a \vec{d} distance apart is positioned. For the nonuniform electrical field, the two charges will face dissimilar values of electric field \vec{E} , and there will be a net force acting on the dipole, as shown in Fig. 2. Now, the sum of the forces on the cell or dielectric particle is given by

$$\vec{F} = q\vec{E}(\vec{r} + \vec{d}) - q\vec{E}(\vec{r}), \quad (1)$$

where \vec{r} represents the position vector of $-q$. So, the electrical field can be written as

$$\vec{E}(\vec{r} + \vec{d}) = \vec{d} \cdot \nabla \vec{E}(\vec{r}) + \vec{E}(\vec{r}). \quad (2)$$

Next

$$\vec{F} = q\vec{d} \cdot \nabla \vec{E}. \quad (3)$$

Next, the electric dipole moment \vec{p} is represented as

$$\vec{p} = q\vec{d}, \quad (4)$$

so the force \vec{F} enforced on the dipole is nothing but the DEP force enforced on the cell or particle

$$\vec{F}_{\text{DEP}} = \vec{p} \cdot \nabla \vec{E}. \quad (5)$$

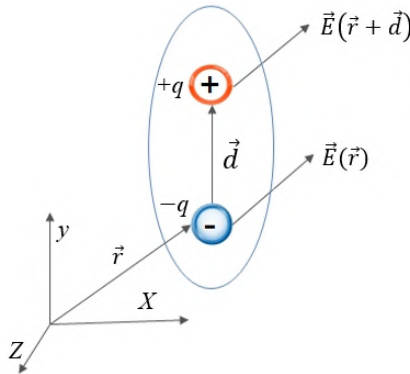


FIG. 2. Amount of net force on the dipole of strength $\vec{p} = q\vec{d}$ in the nonuniform electrical field.

If the cell is suspended in the dielectric fluid medium of permittivity ε_m and exposed to a nonuniform electrical field, a dipole moment is induced on the cell. Then, the electrostatic potential φ_D due to the effective point dipole moment \vec{p}_{eff} is

$$\varphi_D = \frac{\cos \theta}{4\pi\varepsilon_m r^2} (p_{\text{eff}}), \quad (6)$$

where θ and r are the polar angles and radial position, respectively. For the homogeneous dielectric sphere of the cell with radius R and permittivity ε_p , the expression of effective dipole moment is given as follows:

$$\vec{p}_{\text{eff}} = 4\pi\varepsilon_m KR^3\vec{E}. \quad (7)$$

where K is the Clausius–Mossotti factor. For an AC nonuniform electrical field, the effective dipole moment becomes

$$\vec{p}_{\text{eff}} = 4\pi\varepsilon_m^* K(\omega) R^3\vec{E}, \quad (8)$$

and then

$$K(\omega) = \frac{\varepsilon_p^* - \varepsilon_m^*}{\varepsilon_p^* + 2\varepsilon_m^*}, \quad (9)$$

where complex dielectric permittivity of particle and dielectric medium are ε_p^* and ε_m^* , respectively, and the driving frequency is ω . Now,

$$\vec{F}_{\text{DEP}} = 4\pi\varepsilon_m^* K(\omega) R^3\vec{E} \cdot \nabla\vec{E}. \quad (10)$$

Again,

$$2E\nabla E = \nabla E^2. \quad (11)$$

So

$$\vec{F}_{\text{DEP}} = 2\pi\varepsilon_m^* R^3 K(\omega) \nabla E_{\text{rms}}^2. \quad (12)$$

Again,

$$\vec{F}_{\text{DEP}} = 2\pi\varepsilon_m R^3 \text{Re}[K(\omega)] \nabla E_{\text{rms}}^2, \quad (13)$$

where $\varepsilon_m^* = \varepsilon_m + \frac{\sigma_m}{i\omega}$, $\varepsilon_p^* = \varepsilon_p + \frac{\sigma_p}{i\omega}$ and the real part of the Clausius–Mossotti factor becomes

$$\text{Re}[K(\omega)] = \frac{\frac{(\sigma_p - \sigma_m)\omega}{(\sigma_p + 2\sigma_m)} + (\varepsilon_p + 2\varepsilon_m)(\varepsilon_p - \varepsilon_m)}{(\varepsilon_p + 2\varepsilon_m)^2 + \left(\frac{\sigma_p + 2\sigma_m}{\omega}\right)^2}, \quad (14)$$

where σ_p is the electrical conductivity of the particle or cell and σ_m is the electrical conductivity of the dielectric medium. Also, $\text{Re}[K(\omega)]$ varies in the range between -0.5 and 1 . If $\text{Re}[K(\omega)]$ is positive, the particle tends to move toward the high electric field strength region. It is called positive DEP. If $\text{Re}[K(\omega)]$ is negative, the particle tends to move in the direction of the low electrical field

strength area. It is known as negative DEP. Also, from Eq. (14), it can be said that if $\omega \rightarrow 0$,

$$\operatorname{Re}[K(\omega)] \rightarrow \frac{-\sigma_m + \sigma_p}{2\sigma_m + \sigma_p}. \quad (15)$$

If $\omega \rightarrow \infty$, then

$$\operatorname{Re}[K(\omega)] \rightarrow \frac{-\varepsilon_m + \varepsilon_p}{2\varepsilon_m + \varepsilon_p}. \quad (16)$$

From Eq. (13), it can be said that \vec{F}_{DEP} varies with the cubic radius of cells or particles. Therefore, cells with a bigger diameter face a larger amount of DEP force than cells or particles with a smaller diameter. Contradictory, the DEP force also varies proportionally with the squared root mean squared value of the electrical field gradient. The dielectric particles with zero surface net charge in a nonuniform electric field receive DEP force in Eq. (17), agreeing with the proposal of Pohl [15]. The schematic representation of DEP is given in Fig. 3.

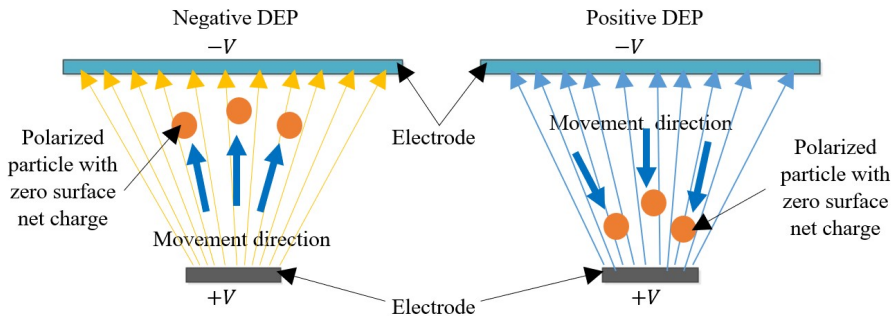


FIG. 3. Schematic representation of the negative and positive DEP.

Different cells have different structures with different dielectric features. Some of these cell structures are equivalent to a solid sphere. Here, the single-shelled-based spherical model is used, as shown in Fig. 4 [16]. The equivalent dielectric permittivity ε_{eq}^* , of this model is

$$\varepsilon_{eq}^* = \varepsilon_s^* \frac{\left(\frac{R_0}{R_i}\right)^3 + \frac{2(\varepsilon_p^* - \varepsilon_s^*)}{\varepsilon_p^* + 2\varepsilon_s^*}}{\left(\frac{R_0}{R_i}\right)^3 - \frac{2(\varepsilon_p^* - \varepsilon_s^*)}{\varepsilon_p^* + 2\varepsilon_s^*}}, \quad (17)$$

where R_0 is the outer radius, R_i is the inner radius of the dielectric shell, ε_p^* is the complex dielectric permittivity of the particle or cell, and ε_s^* is the complex dielectric permittivity of the outer shell.

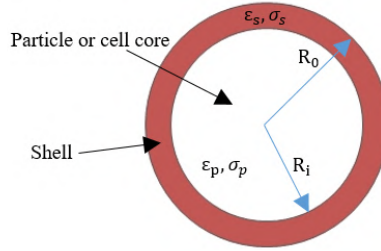


FIG. 4. Spherical cell model with a single shell.

The effectiveness of the microfluidic device is expressed by cells separation efficiency (C_{SE}), cells separation purity (C_{SP}), plasma separation purity (P_{SP}), and plasma separation efficiency (P_{SE}):

$$C_{SE}(X) = \frac{\text{The cell of type } X \text{ reaching the target outlet of } X}{\text{The cell of type } X \text{ injected at the inlet}}, \quad (18)$$

$$C_{SP}(X) = \frac{\text{The cell of type } X \text{ reaching the target outlet of } X}{\text{The cell of all types reaching the target outlet of } X}, \quad (19)$$

$$P_{SP} = 1 - \frac{\text{Number of cells collected at plasma outlet}}{\text{Total number of cells injected at the inlet}}, \quad (20)$$

$$P_{SE} = \frac{\text{Total volume of plasma collected at plasma outlet}}{\text{The total volume of blood injected at the inlet}}. \quad (21)$$

3. PROPOSED MICROFLUIDIC DESIGN STEPS AND SIMULATION MODEL

3.1. Design of the microfluidic platform

Two types of design with flat and curved microchannels with a length of 600 μm and width of 68 μm are used, as shown in Figs. 5 and 6, respectively. These have two inlets. One is used as the blood sample inlet of length 109 μm and width of 38 μm , and the other one is used as the buffer inlet of length 109 μm and width of 68 μm . There are three cell separation outlets at the edge of the microchannel, each has a length of 109 μm and a width of 38 μm . On the upper side of the microchannel, there are six, and at the bottom (lower), there are eleven plasma outlets. Each of these has a length of 95 μm and a width of 16 μm . The electrodes are placed on the upper portion of the microchannel. Two different shapes of micro-tip electrodes, triangular and semicircular micro-tip, are considered, as shown in Fig. 6. Here, these electrodes were designed because of their higher electrical field strength, which is responsible for larger DEP force than the normal shape of electrodes such as triangular, rectangular,

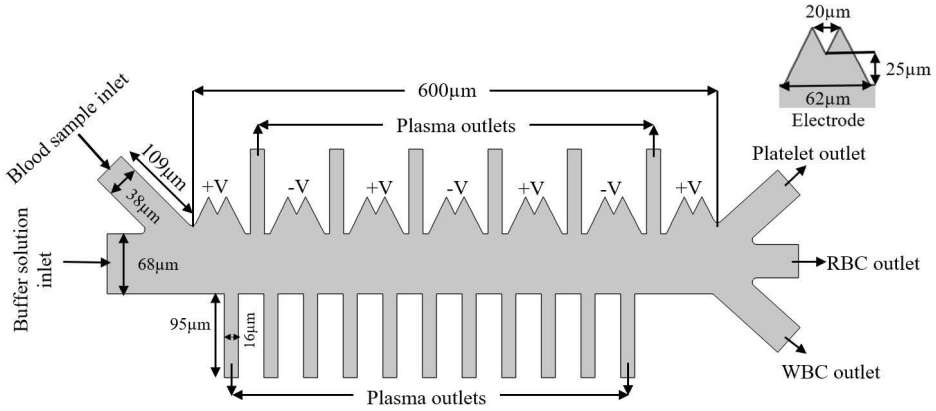
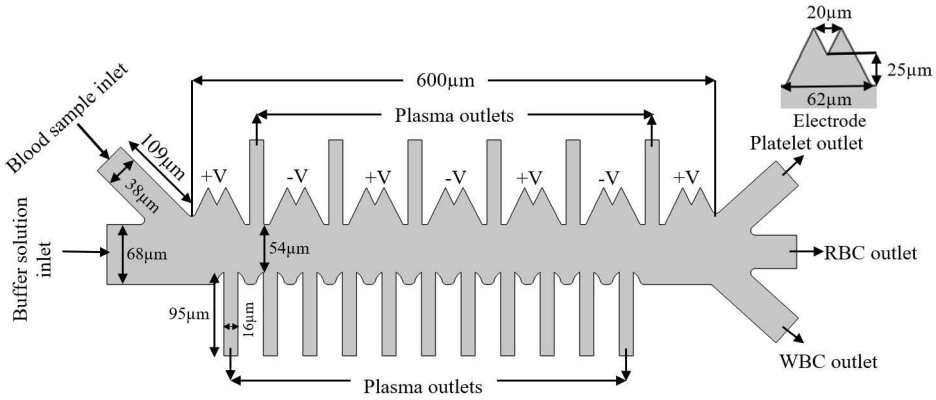


FIG. 5. Design of the device with a flat microchannel.

a)



b)

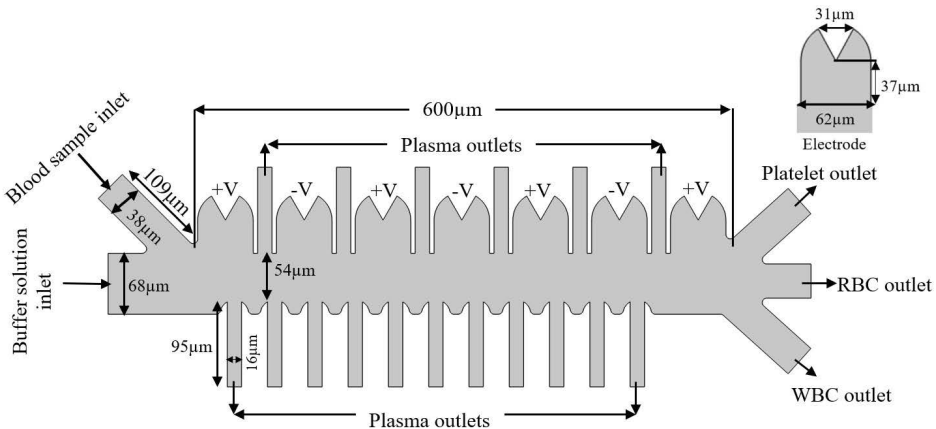


FIG. 6. Design of the device featuring curved microchannel using:
 a) triangular micro-tip, b) semicircular micro-tip electrode.

or semicircular [17, 18]. The electrodes are organized in such a way that applying AC voltage to the electrodes results in a nonuniform electrical field inside the microchannel. The width of both electrodes is 62 μm and the height of the micro-tip to the base for triangular is 20 μm and the semicircular is 37 μm . The inflow velocity at the buffer inlet is maintained higher than the inflow velocity at the blood sample inlet to maintain the focus of the blood particles toward the electrodes. The conductivity of the carrier sample fluid inside the microchannel is achieved at 55 ms/m by diluting the injected blood sample with the help of injected phosphate buffer saline (PBS) solution. The density and dynamic viscosity of the fluid is achieved at 1000 kg/m^3 and 0.001 $\text{Pa}\cdot\text{s}$, respectively. The dielectric properties of three kinds of blood cells and diluted blood plasma are shown in Tables 1 and 2, respectively [18–22].

3.2. Simulation process

3.2.1. Configuring fluid flow. The creeping flow constituent is used for generating the flow field inside the channel. In this flow, inertial forces are smaller than viscous forces. The Reynolds number for this flow is $\text{Re} \ll 1$. The commanding equations of the creeping flow are given as:

$$\nabla \cdot [-PI + K] + F = 0, \quad (22)$$

$$\rho \nabla \cdot u = 0, \quad (23)$$

where P denotes the pressure, I denotes the identity matrix, and u is the velocity vector.

3.2.2. Configuring electrical field. The electrical currents module is used for the electrical field mapping in the device. The equations are given as follows:

$$\nabla \cdot J = Q_{j,v}, \quad (24)$$

$$J = \sigma E + J_e, \quad (25)$$

$$E = -\nabla V, \quad (26)$$

where J is the current density, $Q_{j,v}$ is the resistive loss, and J_e is the externally generated current.

3.2.3. Setting up the particle tracing constituent. In this part, the drag and DEP forces are enforced toward the cells. The commanding equations, which are used for the DEP force, are given in Eqs. (24) and (25). The cells in the blood are formed using single-shelled spherical model, mentioned in Eq. (26).

TABLE 1. Dielectric features of blood cells of type 1 and type 2.

Cells in blood	Blood cells of type 1			Blood cells of type 2		
	PLTs	RBCs	WBCs	PLTs	RBCs	WBCs
Diameter [μm]	1.8	5	9.4	2	6	14
Electrical conductivity [S/m]	2.5e-4	3.1e-4	4.87e-4	0.25	0.31	0.65
Relative permittivity	50	59	136	50	59	60
Shell's electric conductivity [S/m]	1e-9	1e-9	7.25e-9	0.1e-5	0.1e-5	2.74e-5
Shell relative permittivity	6	4.44	10.3	6.7	4.44	6
Shell thickness [nm]	8	9	6.5	8	9	7

TABLE 2. Dielectric features of blood plasma.

Plasma of blood	Diluted plasma
Electric conductivity [mS/m]	55
Relative permittivity	80

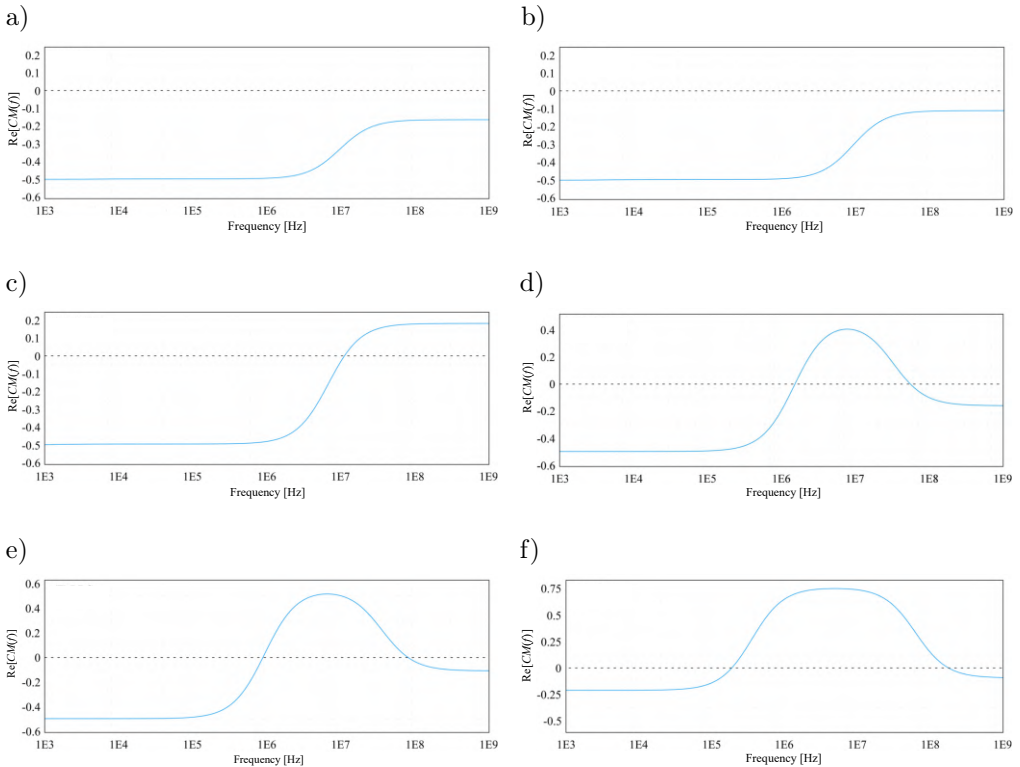


FIG. 7. Plotting of $\text{Re}[CM(f)]$ vs. frequency [Hz] for: a) platelet, b) RBC, c) WBC; and for: d) platelet, e) RBC, f) WBC utilizing Tables 1 and 2 features, respectively.

Based on the dielectric features of the blood cells given in Table 1 and the blood plasma in Table 2, $\text{Re}[K(\omega)]$ or $\text{Re}[CM(f)]$ is analyzed, and the spectrum is shown in Fig. 7. It is found that for both PLTs and RBCs, the negative $\text{Re}[CM(f)]$ exists for all frequencies. But for WBC, the negative $\text{Re}[CM(f)]$ exists in frequencies ranging from 10^3 to 10^6 Hz. Also, at 10^5 Hz all three kinds of blood cells are subjected to maximum negative $\text{Re}[CM(f)]$. So, at this frequency, the maximum negative DEP force can be achieved. Also, based upon the features in Tables 1 and 2, $\text{Re}[CM(f)]$ is analyzed, and the spectrum is shown in Fig. 7. It is found that for both RBCs and WBCs, the negative $\text{Re}[CM(f)]$ exists for the frequency range from 10^3 to 10^5 Hz. But for platelet, the negative $\text{Re}[CM(f)]$ exists for the frequency ranging from 10^3 to 10^6 Hz. So, for applying the negative DEP force to all the blood cells, 10^5 Hz frequency is chosen. Therefore, considering two types of features, the driving frequency is taken as 10^5 Hz or 100 kHz.

In Eq. (13), the DEP force varies with the cell cubic radius, and consequently the WBC comprises the highest diameter subjected to a larger negative DEP force than the RBC and PLT with smaller diameter. As a result, the WBCs will have the highest deflection toward the lower electrical field strength area of the microchannel that is away from the micro-tip and will follow the last (11th) cell outlets. On the other hand, the diameter of the RBC is greater than PLT. So, the RBCs will be subjected to a larger amount of the negative DEP force than the PLT and will deflect toward a smaller electric field strength region and follow the middle cell outlet. The diameter of the PLTs is very small. So, they are subjected to the lower magnitude of the negative DEP force and smaller deflection. Hence, the PLTs will follow the first cell outlet (OLT). The uninterrupted plasma will flow through the lower and upper outlets. Due to the stronger negative DEP force generated by the micro-tip electrodes placed on the upper side, the blood cells will be repelled toward the center of the microchannel, and uninterrupted plasma will flow through the upper side outlets. Also, due to the bifurcation, at the lower side plasma outlets, the flow velocity is smaller than in the middle of the microchannel. So, the blood cells will flow through the center of the microchannel and the plasma will flow through the bottom side outlets.

4. ANALYSIS OF SIMULATION RESULTS

4.1. Impact of microchannel geometry on the flow velocity at the plasma outlets

Two types of microchannel flat and curved-based devices are shown in Figs. 5 and 6, respectively. Initially, the blood sample and buffer solution inlet flow

velocities are maintained at $700 \mu\text{m/s}$ and $1200 \mu\text{m/s}$, respectively. The average flow velocities at the upper and lower plasma outlets are plotted as shown in Fig. 8. One can observe that the curved microchannel geometry results in higher flow velocity at the upper and lower outlets. Therefore, a curved microchannel is selected over the flat microchannel.

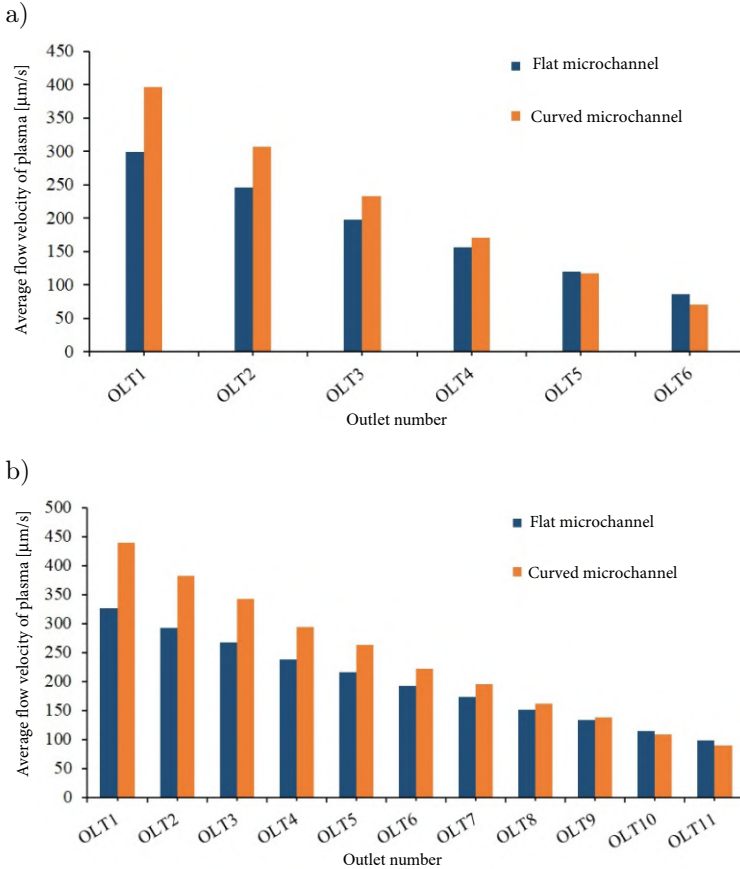


FIG. 8. Plot of average flow velocity at (a) upper and (b) lower plasma outlets.

4.2. Impact of micro-tip electrode's geometrical structure on the electrical field strength in the device

Segregation of distinct cells and plasma inside the microchannel depends on the high DEP force that needs greater electric field strength generated by the electrodes. Triangular and semicircular micro-tip electrodes are designed, as shown in Fig. 6. Initially, $10 V_{pp}$ voltage is applied to the electrodes. The nonuniform electric field distribution inside the device is shown in Fig. 9. It is noted that the extreme electrical field line density is observed at micro-tip point,

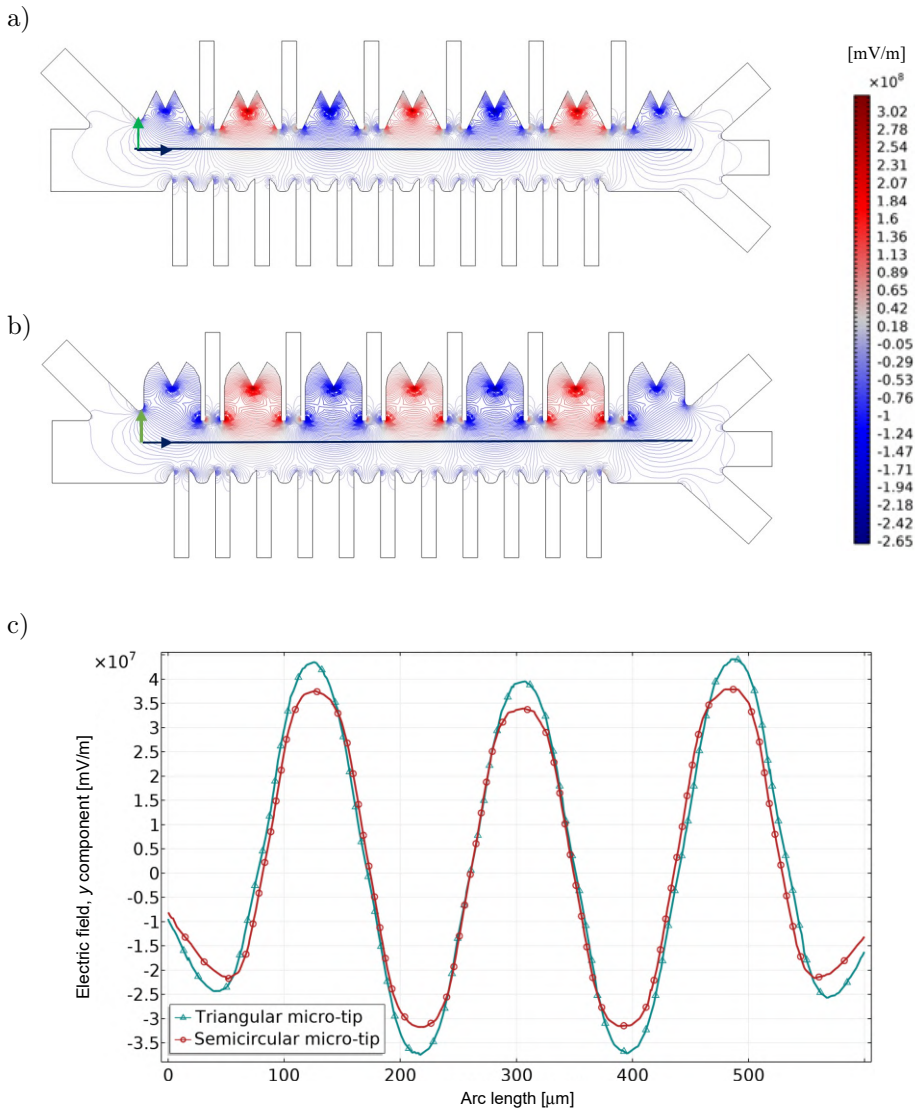


FIG. 9. Electrical field strength map inside the device for: a) triangular micro-tip, b) semicircular microtip electrodes, and c) electrical field strength at the reference cut line.

corners, and in front of both electrodes. Far from the electrodes, the electric field line density reduces, resulting in the reduction of the electric field strength also. A cut line is taken as the reference from $20 \mu\text{m}$ above the middle of the micro-channel, as shown in Fig. 9, to explore which micro-tip electrode geometry delivers higher electrical field strength. It is seen that the electrical field strength for the triangular micro-tip electrode is greater than the semicircular micro-tip at the similar reference cut line location.

The blood particle trajectories are simulated by taking the properties from Table 1, using both these electrodes, as shown in Fig. 10. It can be seen that the separation distance between PLT and RBC trajectories for triangular micro-tip electrodes is about $20\ \mu\text{m}$ and the semicircular micro-tip electrode is about $15\ \mu\text{m}$. Also, the separation distance between RBC and WBC trajectories for triangular micro-tip electrodes is about $32\ \mu\text{m}$ and for the semicircular micro-tip electrode is about $22\ \mu\text{m}$. The larger separation distance reduces the clogging in a microchannel. As a result, the separation efficiency for PLT, RBC, and WBC is 63.93%, 98.9%, and 98.36%, respectively, which is greater than the separation efficiency of the device using semicircular micro-tip electrodes with the separation efficiency of 50.8%, 94.45%, and 95.6%, respectively. Although at the bottom outlets, the plasma separation purity for using both types of electrodes is about 99.45% but the plasma separation purity at the upper outlets for the device us-

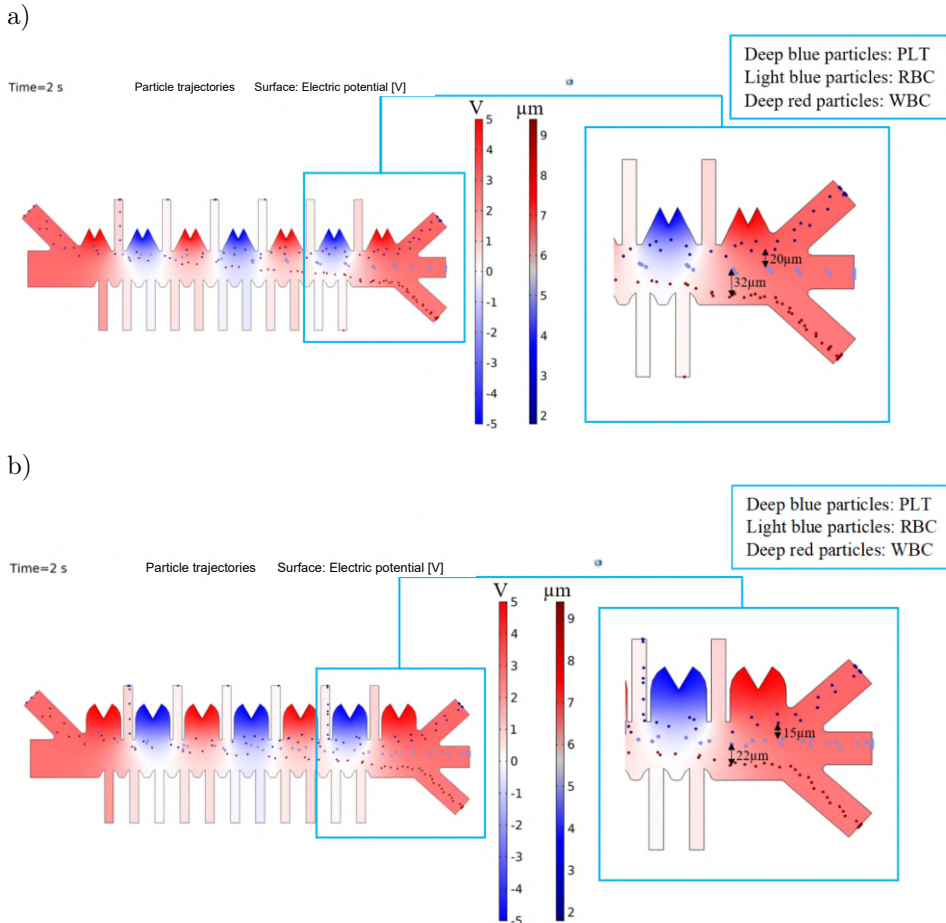


FIG. 10. Separation distance between blood cell trajectories using: a) triangular micro-tip and b) semicircular micro-tip electrodes.

ing triangular micro-tip electrode is 94.35%, which is greater than the device using semicircular micro-tip electrode with the separation purity of 92%. For all of these reasons, triangular micro-tip electrodes are selected.

4.3. Impact of electrode voltage and width of the plasma outlets on the separation performance

The electrical field strength inside the microchannel also varies with the change in applied peak-to-peak voltages on the electrodes. In this section, the separation purities and efficiencies of blood cells and separation purity of plasma are analyzed with the variation of enforced peak-to-peak triangular micro-tip electrode voltage and plasma outlet width, as shown in Figs. 11, 12 and 13. In Fig. 11, it can be observed that using a plasma outlet width of 16 μm , the 100% blood cell separation purity for PLT, WBC, and RBC is achieved at the 10 V_{pp} electrode voltage. The separation efficiency for PLT, RBC, and WBC is 63.93%, 98.9%, and 98.36%, respectively, which is the highest and achieved at 10 V_{pp} electrode voltage. Also, the maximum plasma separation purity at upper and bottom outlets is 94.35% and 99.95%, respectively and achieved at 10 V_{pp} electrode voltage. In this case when the electrode voltage range is less than 10 V_{pp} , due to low electric field strength, less negative DEP force is enforced on the

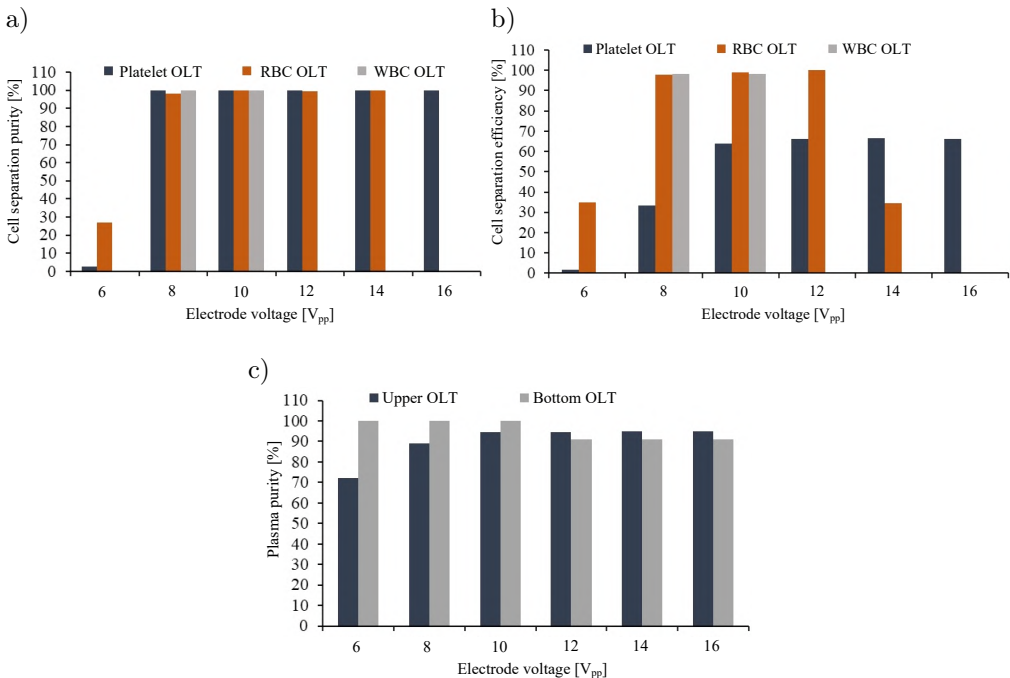


FIG. 11. Plot of a) cell separation purity vs. electrode voltage, b) cell separation efficiency vs. electrode voltage, and c) plasma purity vs. electrode voltage using 16 μm plasma outlet width.

blood cells. As a result, the deflection of RBC and WBC is significantly small, and they are not able to separate, as shown in Fig. 11. For less negative DEP force, a large number of blood cells also reach the upper outlets, resulting in reduced plasma purity. When the electrode voltage range is more than $10 V_{pp}$, for high electric field strength, a larger amount of negative DEP force is enforced on the blood cells.

The deflection of all the blood cells toward the lower electric field strength region is greater. As a result, the separation purity and efficiency of the blood cells is reduced, and a large number of WBCs reach the bottom outlet, resulting in reduced plasma purity. In Fig. 12, it can be seen that considering a plasma outlet width of $14 \mu\text{m}$, the 100% separation purity for PLTs, RBCs, and WBCs is achieved at the $10 V_{pp}$ and $12 V_{pp}$ electrode voltages. The highest separation efficiency for the PLTs, RBCs and WBCs is achieved at $10 V_{pp}$ electrode voltage, which is 65%, 98.36% and 98.9%, respectively. Also, maximum plasma purity for upper and bottom plasma outlets is achieved at $10 V_{pp}$ electrode voltage, which is 94.4% and 100%, respectively.

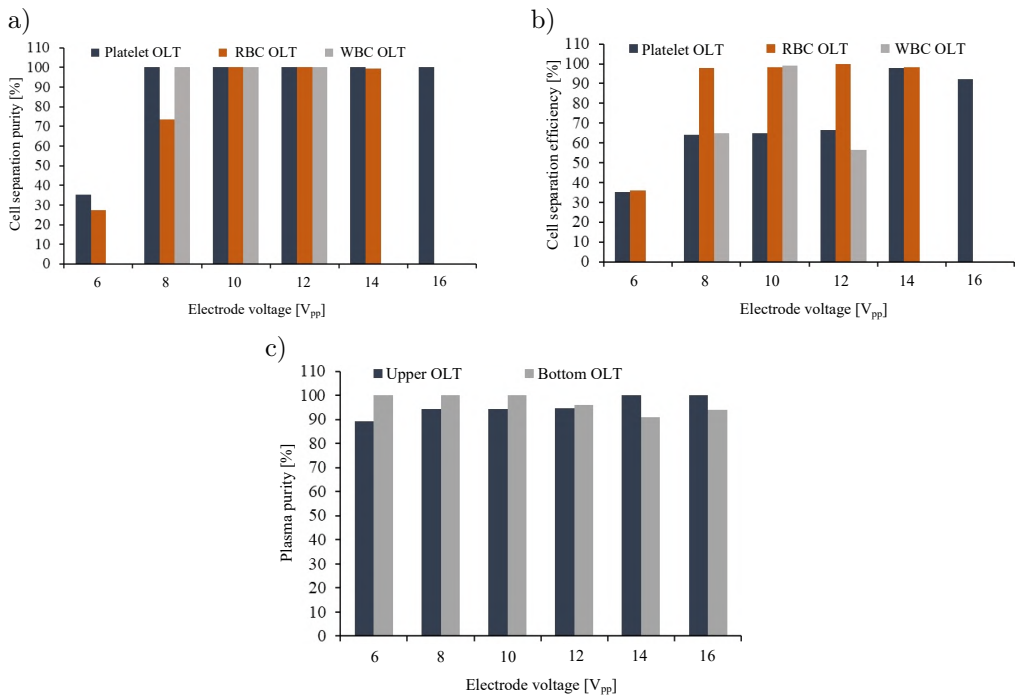


FIG. 12. Plot of a) cell separation purity vs. electrode voltage, b) cell separation efficiency vs. electrode voltage, and c) plasma purity vs. electrode voltage using $14 \mu\text{m}$ plasma outlet width.

When the electrode voltage range is greater than $12 V_{pp}$, for higher electric field strength, the magnitude of negative DEP force is greater. So, the deflection

of all the particles is large, resulting in friction of PLTs with the inner walls and a large deflection of RBCs toward the WBC outlet. Also, the WBCs in the bottom plasma outlets reduce the plasma purity. In Fig. 13, it can be noted that considering 12 μm plasma outlet width, 100% cell separation purity at the three kinds of cell outlets is achieved at 10 V_{pp} and 12 V_{pp} electrode voltages. Optimum cell separation efficiency is achieved at 12 V_{pp} electrode voltage, which is 99.45% for the PLT outlet, 100% for both RBCs and WBCs outlets, and 100% purified plasma at the lower and upper plasma outlets is accomplished at 10 V_{pp} and 12 V_{pp} electrode voltages. In Fig. 14, it can also be observed that when the electrode voltage is 8 V_{pp} , the amount of the negative DEP force acting on the blood cells is very small. So, smaller deflection of WBCs results in clogging and friction with the inside wall of the RBC outlet. Also, the RBCs get clogged and have friction with the inside wall of its outlet, affecting the separation efficiency. The WBCs and RBCs are not separated and come through the same RBC outlet affecting the separation purity as well. On the other hand, due to less force, the deflection of the PLTs is significantly smaller, resulting in PLTs entering the upper outlets and affecting the plasma purity. When the electrode voltage is more than 12 V_{pp} , taking 16 V_{pp} electrode voltage, due to higher electrical field strength, the higher negative DEP force acting on WBCs results

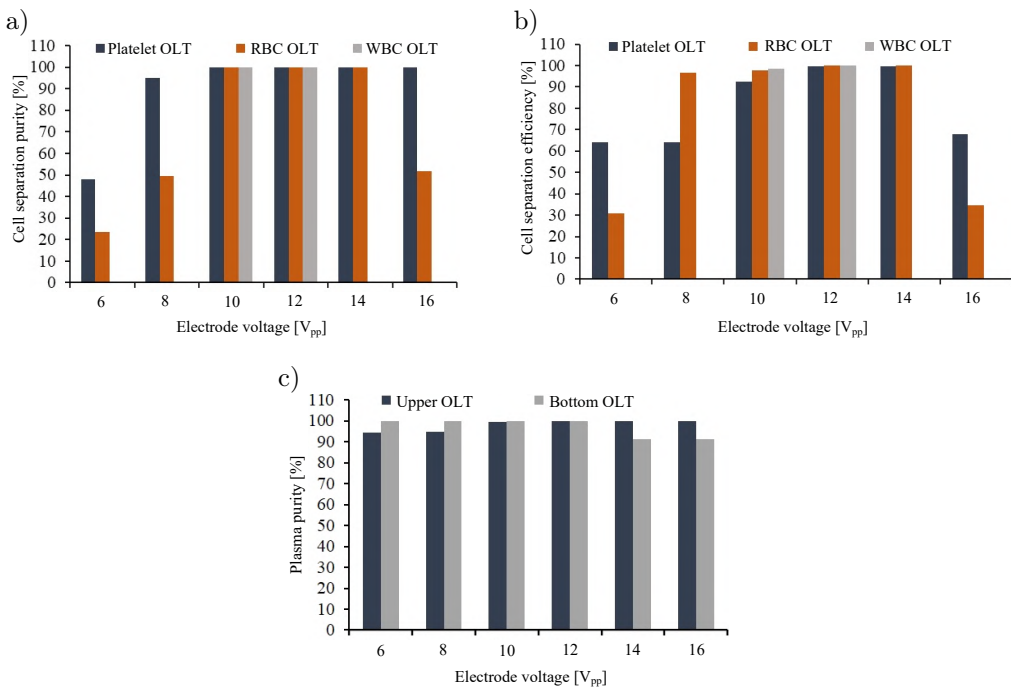


FIG. 13. Plot of a) cell separation purity vs. electrode voltage, b) cell separation efficiency vs. electrode voltage, and c) plasma purity vs. electrode voltage using 12 μm plasma outlet width.

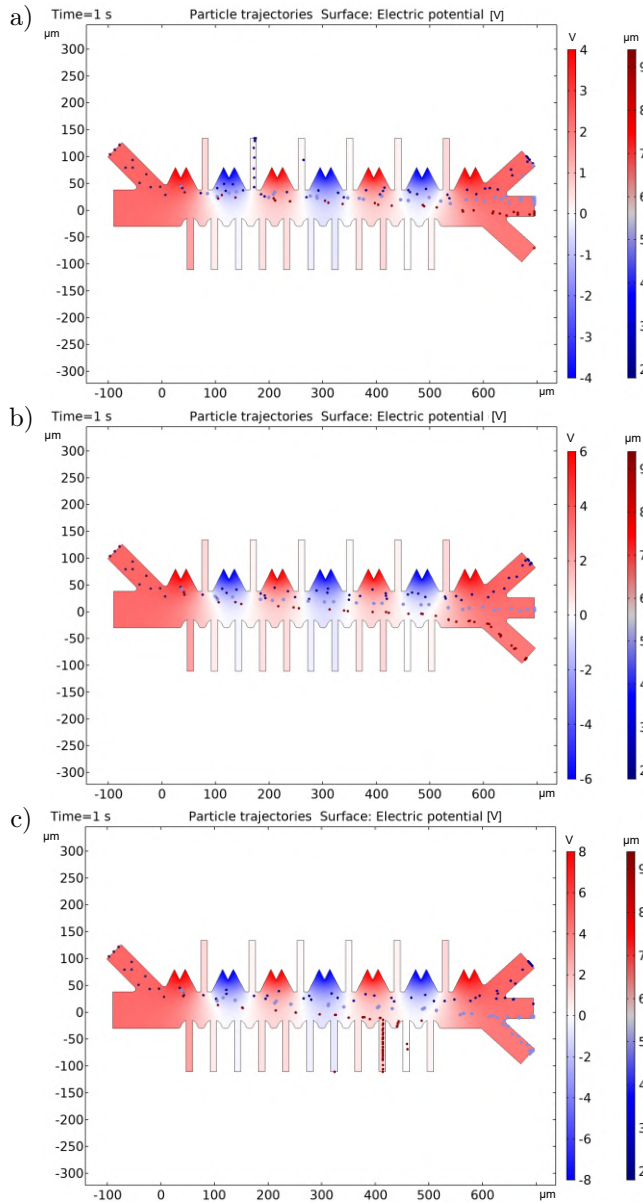


FIG. 14. Separation at: a) $8 V_{pp}$, b) $12 V_{pp}$, and c) $16 V_{pp}$ electrode voltages using $12 \mu\text{m}$ width of plasma outlets.

in the flow toward bottom outlets and clogging in the bottom wall. Therefore, plasma purity is reduced.

Therefore, it can be observed that maximum cell isolation purity and efficiency, and plasma purity are achieved with $12 V_{pp}$ electrode voltage and $12 \mu\text{m}$

width of plasma outlets. The amount of negative DEP forces acting on blood cells at the different positions inside the device is shown in Table 3. Also, taking these design parameters into account, the particle trajectories for the particle properties of type 2, shown in Table 1, are simulated and the simulation result is shown in Fig. 15. At 12 V_{pp} electrode voltage, the device can achieve cells

TABLE 3. Amount of negative DEP force enforced on the blood cells of type 1 and type 2 properties.

PLT position (x) [μm]	PLT position (y) [μm]	DEP force on platelet [pN]	RBC position (x) [μm]	RBC position (y) [μm]	DEP force on RBC [pN]	WBC position (x) [μm]	WBC position (y) [μm]	DEP force on WBC [pN]
Blood cells of type 1 properties								
35.162	45.750	-0.24351	131.28	27.759	-5.2027	105.47	17.512	-24.380
42.470	34.843	-0.11597	184.32	23.107	-4.3966	137.28	17.677	-19.177
103.04	25.469	-0.33107	206.36	21.273	-2.8816	147.50	14.359	-15.096
274.75	23.766	-0.23018	303.19	18.387	-2.6258	216.51	10.201	-9.1832
559.47	21.890	-0.10706	396.05	15.321	-1.9551	244.60	8.1274	-9.2092
35.162	45.750	-0.24351	484.24	12.752	-2.2359	254.92	6.3983	-7.9129
42.470	34.843	-0.11597	533.64	7.6812	-1.6929	312.10	4.2051	-6.7843
Blood cells of type 2 properties								
116.04	43.014	-0.65811	108.99	27.720	-9.9772	105.63	20.222	-27.032
120.89	34.986	-0.49410	135.06	24.737	-7.4348	141.67	19.739	-20.385
194.18	25.423	-0.29714	203.60	22.783	-5.6717	214.52	15.138	-11.905
425.79	22.312	-0.23844	210.19	19.021	-4.1815	248.31	11.912	-11.302
352.96	21.972	-0.19316	235.96	18.119	-4.5116	314.34	9.7929	-9.4739
565.51	22.003	-0.12085	333.79	13.123	-3.5564	346.09	7.1534	-8.0087
597.91	30.985	-0.035503	425.18	10.050	-2.3582	404.25	5.8441	-6.1161

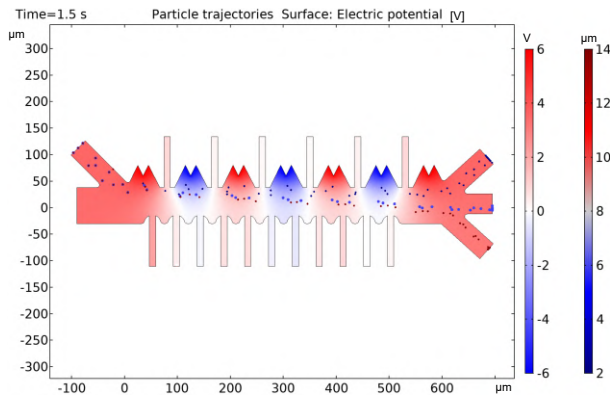


FIG. 15. Separation at 12 V_{pp} electrode voltage using 12 μm width of plasma outlets.

separation purity of 100% and the separation efficiencies of 97%, 98.9%, and 98.36% at the PLT, WBC, and RBC outlets, respectively. Also, 100% purified plasma is achieved at both upper and lower plasma outlets. The amount of negative DEP forces acting on the blood cells at the different positions inside the device is shown in Table 3. It can be observed that regions near the electrodes and the larger blood cell diameter are subjected to the larger negative DEP force than away from the electrodes and the smaller blood cell diameter.

4.4. Effectiveness of the blood sample and buffer solution inlets flow velocities on the separation efficacy of the device

The velocities at the blood sample and the buffer solution inlets vary considering blood cells of properties of type 1 in Table 1 and using design parameters obtained in the previous section at 12 V_{pp} electrode voltage. The impact of flow velocity on the separation performance of the device can be analyzed in Fig. 16. The optimum separation performance is achieved at the flow velocity range from 700–1100 $\mu\text{m/s}$ at the inlet of the blood sample and the flow velocity range of

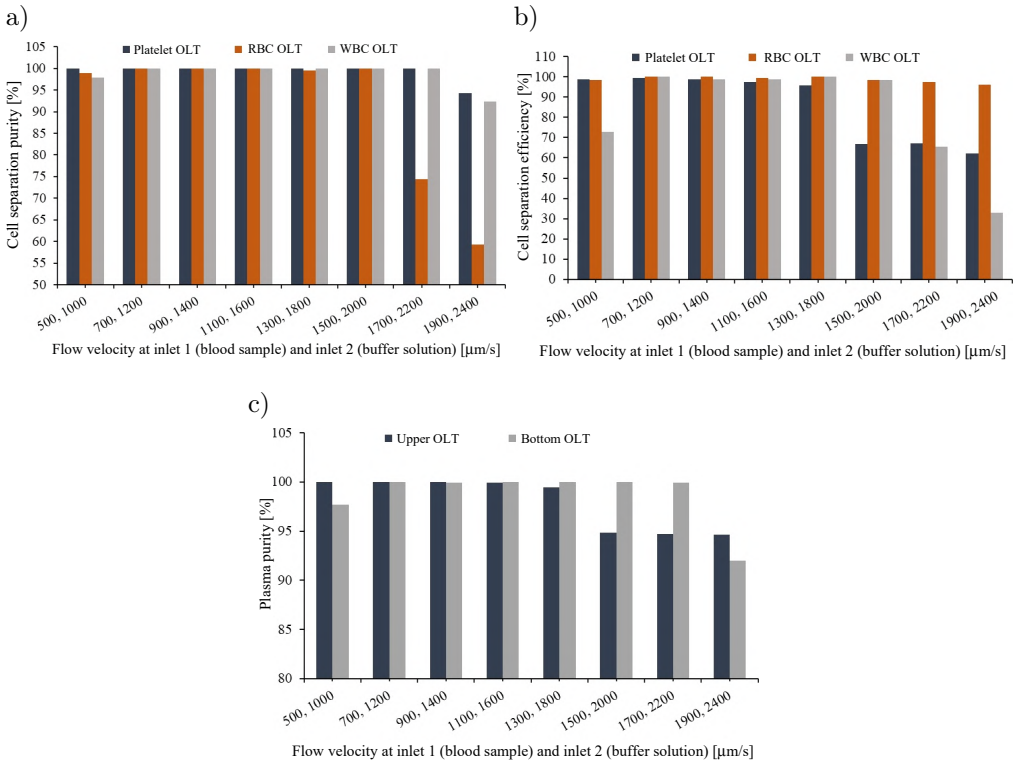


FIG. 16. Plot of a) cell separation purity, b) cell separation efficiency, and c) plasma purity vs. flow velocity at inlet 1 (blood sample) and inlet 2 (buffer solution).

1200–1600 $\mu\text{m/s}$ at the buffer inlet. However, using 700 $\mu\text{m/s}$ flow velocity at the inlet of the blood sample, the mass flow rate achieved is 2.793×10^{-11} kg/s and the volumetric flow rate is 2.66×10^{-14} m^3/s .

Also, using 1200 $\mu\text{m/s}$ flow velocity at the buffer solution inlet, the mass flow rate achieves 8.16×10^{-11} kg/s and the volumetric flow rate is 8.16×10^{-14} m^3/s . The diluted plasma flow rate achieved at the upper plasma outlets range from 5.44752×10^{-15} m^3/s to 1.087944×10^{-15} m^3/s and at the bottom plasma outlets range from 5.86164×10^{-15} m^3/s to 1.37748×10^{-15} m^3/s . So, the diluted plasma separation efficiency is achieved at 52.33%. However, using 1100 $\mu\text{m/s}$ flow velocity at the blood sample inlet, the mass flow rate achieved 4.389×10^{-11} kg/s the volumetric flowrate calculated at the blood sample inlet is 4.18×10^{-14} m^3/s . Also, using 1600 $\mu\text{m/s}$ flow velocity at the buffer solution inlet, the mass flow rate achieved 1.088×10^{-10} kg/s and the flow rate calculated at the buffer solution inlet is 1.088×10^{-13} m^3/s . The diluted plasma flow rate achieved at the upper plasma outlets ranges from 7.57908×10^{-15} m^3/s to 1.51368×10^{-15} m^3/s and at the bottom plasma outlets ranges from 8.15532×10^{-15} m^3/s to 1.9164×10^{-15} m^3/s . Therefore, the plasma separation efficiency is achieved at 52.31%. Now, it can be observed that in both cases, the plasma separation efficiency is almost equal as the velocity increases in a similar increment ratio. However, for maintaining the low pressure inside the device the smaller flow velocity at the inlets is chosen as 700 $\mu\text{m/s}$ blood sample inlet flow velocity and 1200 $\mu\text{m/s}$ buffer solution inlet flow velocity. Also, considering the blood cell properties of type 2 from Table 1, at 700 $\mu\text{m/s}$ blood sample inlet flow velocity and 1200 $\mu\text{m/s}$ buffer solution inlet flow velocity, the maximum diluted plasma separation efficiency is achieved at 52.33%.

5. CONCLUSION

The research analysis on microfluidic design for continuous separation of three kinds of blood cells and plasma explored the influence of DEP. We have successfully investigated various microchannel geometries, electrode shapes, electrode voltages, widths of plasma outlets, and flow velocities at the inlets to compute their effect on blood cell isolation purity and efficacy, plasma segregation purity and efficiency, and plasma flow velocity through simulation in COMSOL Multiphysics 5.4 software. The design featuring curved microchannel, triangular micro-tip electrodes, and 12 μm plasma outlet width was able to perform successful separation of all three kinds of blood cells with two types of properties and plasma at 12 V_{pp} electrode voltage and at 700 $\mu\text{m/s}$ blood sample inlet flow velocity and 1200 $\mu\text{m/s}$ buffer solution inlet flow velocity. The device efficiently produced 100% cells separation purity and cells separation efficiency of 99.45% for the PLT outlet, 100% for both RBCs and WBCs outlets, 100%

purified plasma at the lower and upper outlets, and plasma separation efficiency of 52.3% considering cell properties of type 1. Also, the device successfully attained 100% cells separation purity and separation efficiencies of 97%, 98.36%, and 98.9% at the PLTs outlet, RBCs outlet, and WBCs outlets, respectively, and 100% purified plasma at both lower and upper outlets, and overall diluted plasma separation efficiency of 52.33% considering cell properties of type 2. Also, from the numerical analysis and considering the spectrums of $\text{Re}[CM(f)]$ for three kinds of cells using two sets of properties, the driving frequency was chosen as 100 kHz. Thus, the device was better suited for the continuous separation of all the blood components compared with existing designs. Moreover, the effectiveness of the device is that it not only separates the diluted plasma but is also able to separate distinct blood cells with various properties. Therefore, it can be used in various clinical point-of-care diagnosis with its superior performance, including efficient separation purity, separation efficiency, and less operating voltage.

ACKNOWLEDGEMENTS

We convey our thanks to Bio-MEMS Laboratory, National Institute of Technology Nagaland, Dimapur-797103, for contributing the simulation tool and ongoing assistance for this research project.

REFERENCES

1. Y.T. Yeh, M. Nisic, X. Yu, Y. Xia, S.Y. Zheng, Point-of-care microdevices for blood plasma analysis in viral infectious diseases, *Annals of Biomedical Engineering*, **42**(11): 2333–2343, 2014, doi: 10.1007/s10439-014-1044-2.
2. R. Harwood, Cell separation by gradient centrifugation, *International Review of Cytology*, **38**: 369–403, 1974, doi: 10.1016/S0074-7696(08)60930-4.
3. G.M. Whitesides, The origins and the future of microfluidics, *Nature*, **442**(7101): 368–373, 2006, doi: 10.1038/nature05058.
4. S.O. Catarino, R.O. Rodrigues, D. Pinho, J.M. Miranda, G. Minas, R. Lima, Blood cells separation and sorting techniques of passive microfluidic devices: From fabrication to applications, *Micromachines*, **10**(9): 593, 2019, doi: 10.3390/mi10090593.
5. E.L. Jackson, H. Lu, Advances in microfluidic cell separation and manipulation, *Current Opinion in Chemical Engineering*, **2**(4): 398–404, 2013, doi: 10.1016/j.coche.2013.10.001.
6. D.R. Gossett *et al.*, Label-free cell separation and sorting in microfluidic systems, *Analytical and Bioanalytical Chemistry*, **397**(8): 3249–3267, 2010, doi: 10.1007/s00216-010-3721-9.
7. S. Karthick, A.K. Sen, Improved understanding of acoustophoresis and development of an acoustofluidic device for blood plasma separation, *Physical Review Applied*, **10**(3): 034037, 2018, doi: 10.1103/PhysRevApplied.10.034037.
8. S. Yan, J. Zhang, G. Alici, H. Du, Y. Zhu, W. Li, Isolating plasma from blood using a dielectrophoresis-active hydrophoretic device, *Lab on a Chip*, **14**(16): 2993–3003, 2014, doi: 10.1039/C4LC00343H.

9. F. Yang *et al.*, Extraction of cell-free whole blood plasma using a dielectrophoresis-based microfluidic device, *Biotechnology Journal*, **14**(3): 1800181, 2019, doi: 10.1002/biot.201800181.
10. M.G. Lee *et al.*, Inertial blood plasma separation in a contraction–expansion array microchannel, *Applied Physics Letters*, **98**(25): 253702, 2011, doi: 10.1063/1.3601745.
11. L. Spigarelli *et al.*, A passive two-way microfluidic device for low volume blood-plasma separation, *Microelectronic Engineering*, **209**: 28–34, 2019, doi: 10.1016/j.mee.2019.02.011.
12. Y. Zhang, X. Chen, Dielectrophoretic microfluidic device for separation of red blood cells and platelets: A model-based study, *Journal of the Brazilian Society of Mechanical Sciences and Engineering*, **42**(2): 89, 2020, doi: 10.1007/s40430-020-2169-x.
13. H. Shirinkami, G. Wang, J. Park, J. Ahn, Y. Choi, H. Chun, Red blood cell and white blood cell separation using a lateral-dimension scalable microchip based on hydraulic jump and sedimentation, *Sensors and Actuators B: Chemical*, **307**: 127412, 2020, doi: 10.1016/j.snb.2019.127412.
14. R.R. Pethig, *Dielectrophoresis: Theory, Methodology and Biological Applications*, John Wiley & Sons, 2017.
15. M. Mischel, F. Rougé, I. Lamprecht, C. Aubert, G. Prota, Dielectrophoresis of malignant human melanocytes, *Archives of Dermatological Research*, **275**(3): 141–143, 1983, doi: 10.1007/BF00510042.
16. I. Turcu, C.M. Lucaciu, Dielectrophoresis: a spherical shell model, *Journal of Physics A: Mathematical and General*, **22**(8): 985, 1989, doi: 10.1088/0305-4470/22/8/014.
17. Y. Kang, D. Li, S.A. Kalams, J.E. Eid, DC-Dielectrophoretic separation of biological cells by size, *Biomedical Microdevices*, **10**(2): 243–249, 2008, doi: 10.1007/s10544-007-9130-y.
18. M.Z.A. B.I., V. Tirth, C.M. Yousuff, N.K. Shukla, S. Islam, K. Irshad, K.O. Aarif, Simulation guided microfluidic design for multitarget separation using dielectrophoretic principle, *BioChip Journal*, **14**(4): 390–404, 2020, doi: 10.1007/s13206-020-4406-x.
19. Y. Zhang, X. Chen, Blood cells separation microfluidic chip based on dielectrophoretic force, *Journal of the Brazilian Society of Mechanical Sciences and Engineering*, **42**(4): 206, 2020, doi: 10.1007/s40430-020-02284-8.
20. M.S. Maria, T.S. Chandra, A.K. Sen, Capillary flow-driven blood plasma separation and on-chip analyte detection in microfluidic devices, *Microfluidics and Nanofluidics*, **21**(4): 72, 2017, doi: 10.1007/s10404-017-1907-6.
21. H. Ali, C.W. Park, Numerical study on the complete blood cell sorting using particle tracing and dielectrophoresis in a microfluidic device, *Korea-Australia Rheology Journal*, **28**(4): 327–339, 2016, doi: 10.1007/s13367-016-0033-4.
22. N.V. Nguyen, T. Le Manh, T.S. Nguyen, V.T. Le, N. Van Hieu, Applied electric field analysis and numerical investigations of the continuous cell separation in a dielectrophoresis-based microfluidic channel, *Journal of Science: Advanced Materials and Devices*, **6**(1): 11–18, 2021, doi: 10.1016/j.jsamd.2020.11.002.

*Received June 16, 2022; revised version November 7, 2022;
accepted November 8, 2022.*